Effect of overflow nappe non-aeration on tsunami breakwater failure

Patil, Akshay; Mudiyanselage, Sanduni Disanayaka; Bricker, Jeremy D.; Uijttewaal, Wim; Keetels, Geert

DOI
10.9753/icce.v36.papers.18

Publication date
2018

Document Version
Final published version

Published in
Proceedings of the Coastal Engineering Conference

EFFECT OF OVERFLOW NAPPE NON-AERATION ON TSUNAMI BREAKWATER FAILURE

Akshay Patil[1], Sanduni Disanayaka Mudiyanselage[1], Jeremy D. Bricker [2,3], Wim Uijttewaal[1], Geert Keetels[4]

Sliding force and punching pressure were contributing factors to widespread breakwater damage caused during the 2011 Great East Japan Tsunami (Takagi and Bricker, 2015), and were dominant factors causing displacement of caissons from the world's deepest breakwater: the Kamaishi bay-mouth composite tsunami breakwater (Arikawa et al., 2012; Bricker et al., 2013). The current study focuses on understanding the physics necessary to correctly model the problem of breakwater over-topping by tsunami. To effectively model the physical behavior of the system, scaled model studies were carried out by Mudiyanselage (2017). The earlier numerical investigations carried out by Bricker et al. (2013) and Mudiyanselage (2017), did not prove conclusive to numerically model tsunami breakwater overflow using OpenFOAM employing a 2-D modeling approach. This was shown to be a major hurdle in prediction of the sliding force on the caisson due to the inability of modeling the non-aerated overflow jet over the caisson. Validation of the numerical model would allow parametric study of the flow physics for varying overflow conditions. As a result, a threefold approach of experimental model, analytical model, and numerical model studies was proposed. To achieve sufficient reliability and have complete flexibility, OpenFOAM was chosen for the numerical setup. This numerical model was used to validate the experiments carried out by Mudiyanselage (2017). The numerical model validates and reproduces the flow physics very well. Overall, the numerical results indicate that non-aeration could provide about 8-19% additional force. It was observed that the force on the caisson has a periodic fluctuating behavior. Additionally, the aeration mechanism and overflow jet breakup during the flow was also investigated. It was observed that the highly 3-dimensional behavior of the overflow jet results in the aeration of the cavity underneath the jet. This also explains why the previous studies Bricker et al. (2013) and Mudiyanselage (2017) failed to correctly model the overflow jet using a 2-D modeling approach.

Keywords: Tsunami; Breakwater Over-topping; Computational Fluid Dynamics; OpenFOAM; Caisson Sliding Failure

INTRODUCTION

During a tsunami event, the stability of a caisson breakwater can be compromised due to the overflow jet. If the foundation of the caisson does not have sufficient strength, a strong horizontal force can destabilize the caisson and result in sliding failure (Takahashi et al., 2014). The dynamics of the overflow jet lead to a pressure reduction on the landward side of the caisson due to non-aeration of the cavity below the nappe. This results in generation of an additional horizontal force, which increases the net horizontal force acting on the caisson. The estimation of this horizontal force and the physical mechanism leading to this condition are imperative in understanding the overall stability of the caisson breakwater during such an overflow tsunami event. Though countermeasures such as the use of friction mats between the caisson and the rubble mound (Suppasri et al., 2018), elevation of the rubble mound itself on the landward side of the caisson, and porous armor units (Mitsui et al., 2014) are being implemented to prevent composite breakwater failure in future tsunamis, determination of the pertinent failure mode (i.e., scour vs. sliding failure vs. foundation bearing capacity failure) is necessary to ensure correct application of these countermeasures. This research investigates the link between cavity sub-pressure under a non-aerated nappe, nappe kinematics, and dynamics.

During the 2011 Great Eastern Japan tsunami, the world's deepest offshore breakwaters, built in the Kamaishi bay (Iwate Prefecture, Japan) partially failed. The breakwater comprised of a pair of breakwaters of lengths 990 m and 670 m linked with a submerged 300 m wide opening (see Figure 1). The tsunami event lead to the displacement of the caisson blocks towards the landward direction. Even the caissons which did not undergo sliding, were not correctly positioned anymore (Arikawa et al., 2012). This confirmed the partial failure of the breakwater due to the tsunami event (Mudiyanselage, 2017).

[1]Environmental Fluid Mechanics Section, Department of Hydraulic Engineering, Faculty of Civil Engineering and Geosciences, Delft University of Technology, Netherlands

[2]Corresponding Author: J.D.Bricker@tudelft.nl

[3]Hydraulic Structures and Flood Risk Section, Department of Hydraulic Engineering, Faculty of Civil Engineering and Geosciences, Delft University of Technology, Netherlands

[4]Offshore and Dredging Engineering Section, Department of Mechanical Engineering and Marine Technology, Delft University of Technology, Netherlands

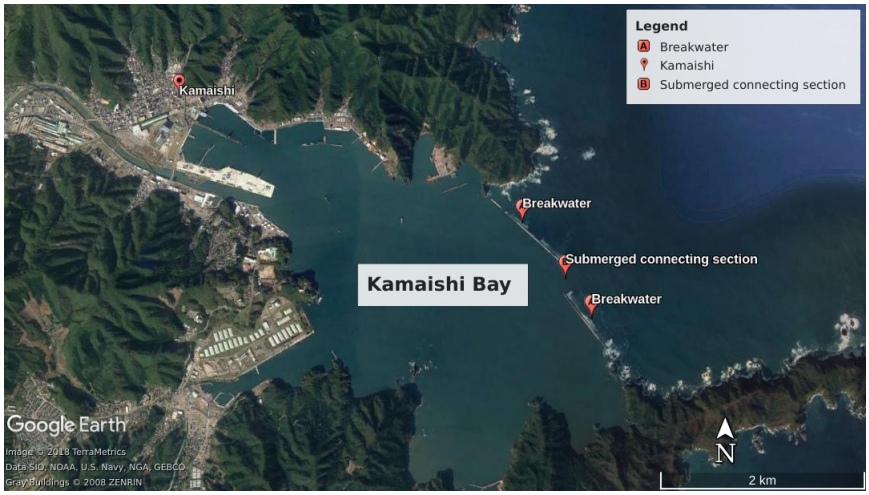

Figure 1: Kamaishi bay along with its breakwaters. The two breakwaters are separated by a submerged connecting section.

In order to understand the overflow jet dynamics, a rigorous procedure involving experimental model, analytical model and Computational Fluid Dynamics (CFD) model studies were proposed. The studies carried out by Bricker et al. (2013) and Mudiyanselage (2017) could not provide information about sliding force in the numerical model due to the inability to model non-aerated overflow using a 2-D model. To correctly model the flow behavior, the experimental studies carried out by Mudiyanselage (2017) were used to validate the numerical model. This validation routine allowed parametric study of the overflow jet.

An introduction to the experimental and analytical formulations by Mudiyanselage (2017) is first provided as a background to the assessment of the numerical model studies. This is followed by a brief introduction to the numerical model investigations presented in this study. The results and conclusions are presented next along with some details about the numerical results. An explanation for the aeration process of the cavity is also included in this section. Finally, some conclusions for further numerical investigations have been recommended along with the implications of using the current model.

METHODOLOGY

This section presents the different approaches used in order to investigate the overflow jet behavior due to non-aeration.

Ballistic model

A simplified tsunami was modeled in the laboratory as a steady breakwater overflow discharge (Mudiyanselage, 2017). A situation sketch for the caisson stability and the hydrostatic pressure distribution acting on the caisson can be seen in Figure 2. There are mainly two conditions of the overflow jet that exist: the aerated and non-aerated cases. The various stages of the nappe under the overflow jet have been classified based on the ventilation of the space (cavity) under the overflow jet (Abdalla and Shamaa, 2016). The current experimental studies only focus on the free nappe (aerated) and the depressed nappe (non-aerated). The sub-atmospheric pressure in the non-aerated case results in the additional force on the caisson.

In order to have an analytical model of the problem, a ballistic model was used by Mudiyanselage (2017) to study the overflow jet trajectory for the aerated and the non-aerated scenarios (see Figure 3), building on the theory of Chanson (1996). In this model, the flow condition is considered to be aerated when the upper and the lower nappe (see Figure 2) are subjected to atmospheric pressure (Mudiyanselage, 2017). The model assumptions are as listed below.

- The only external force on the nappe is gravitational.
- At the brink of the caisson, only the horizontal component of the velocity vector exists.

- The horizontal velocity component of flow is constant until the jet impinges the water level under the cavity.

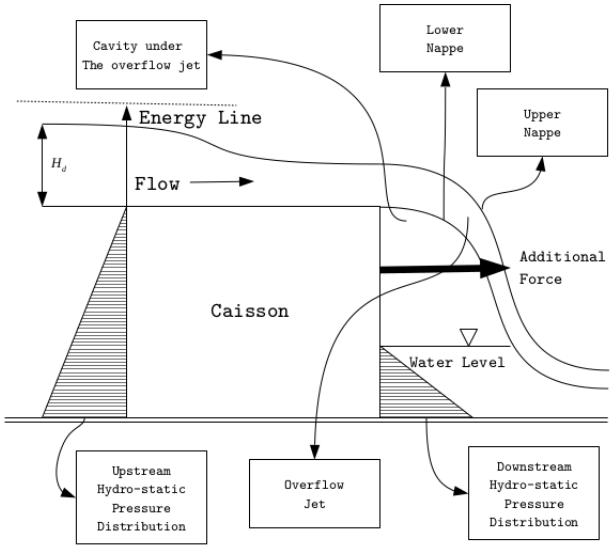

Figure 2: Situation sketch of the caisson during a steady overflow event.

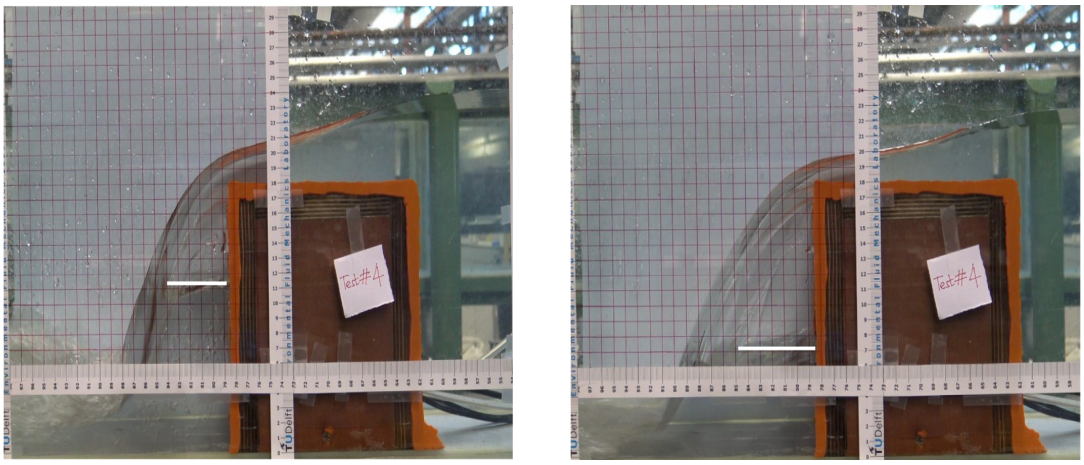

(a) Non-aerated nappe **(b) Aerated nappe**

Figure 3: Behavior of the overflow jet trajectory in the two cases. Overflow discharge, $Q = 0.00405$ $[m^3/s]$. The white lines indicate the water level in the cavity (Mudiyanselage, 2017).

The water particle is considered to be in the lower surface of the nappe (lower part of the overflow jet). The co-ordinate system is so chosen that x is positive in the flow direction while y is positive in the downward direction. As the horizontal component is constant, the vertical thickness of the nappe ($d_{vertical}$) can be assumed to be constant (Chow, 2009). As the obtained equations are quadratic, theoretically a parabolic profile of the upper and the lower nappe are to be expected. The model for aerated flow (with the above mentioned assumptions) is as presented below (Mudiyanselage, 2017),

$$\frac{y}{H} = A(\frac{x}{H})^2 + \frac{d_{vertical}}{H}, \tag{1}$$

where H is the total energy head, y is the y co-ordinate (position), and $A = \frac{gH}{u^2}$.

In order to derive the non-aerated nappe trajectory using a ballistics model, an additional mechanism which accommodates for the lowering of pressure under the overflow jet was incorporated by Mudiyanselage (2017). This mechanism includes additional acceleration (a_i) due to the pressure drop inside the cavity with respect to the atmospheric pressure. This acceleration acts perpendicular to the lower nappe envelope. The water particle under consideration exists in the lower surface of the nappe (see Figure 2). The nappe parameters for the non-aerated case can be seen in Figure 4. The additional acceleration due to the pressure drop can be formulated as described in Equation 2 where ΔP $[Pa]$ is the pressure drop across the overflow jet, d_i $[m]$ is the thickness of the jet, and ρ $[kg/m^3]$ is the fluid density (see Figure 4). Additionally, the nappe thickness gradually reduces along the projectile path from the top of the caisson to the impingement point to maintain continuity. This is due to the increasing vertical velocity along the trajectory and as a result, the thickness of the nappe is reduced to maintain a constant flow rate (Mudiyanselage, 2017). Based on the above discussion, the final analytical model is as expressed in Equations 2-8. The length scales are defined in Figure 4, with the x axis positive in flow direction and y axis positive upwards, while u and v correspond to the velocity in x and y directions respectively.

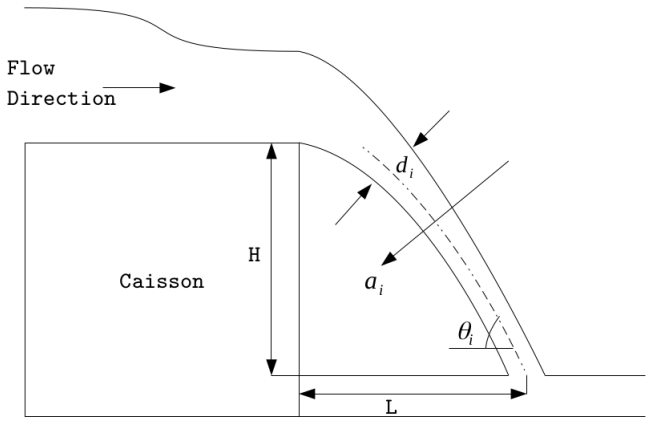

Figure 4: Nappe trajectory with additional acceleration due to cavity sub-pressure.

$$a_i = \frac{\Delta P}{\rho d_i} \tag{2}$$

$$\Delta x_i = u_{i-1} \cdot \Delta t - \frac{1}{2} \cdot (a_{i-1} \cdot sin(\theta_{i-1})) \cdot \Delta t^2 \tag{3}$$

$$u_i^2 = u_{i-1}^2 - 2 \cdot (a_{i-1} \cdot sin(\theta_{i-1})) \cdot \Delta x_i \tag{4}$$

$$\Delta y_i = -v_{i-1} \cdot \Delta t + \frac{1}{2} \cdot (g + a_{i-1} \cdot cos(\theta_{i-1})) \cdot \Delta t^2 \tag{5}$$

$$v_i^2 = v_{i-1}^2 + 2 \cdot (g + a_{i-1} \cdot cos(\theta_{i-1})) \cdot \Delta y_i \tag{6}$$

$$d_i = \frac{Q}{B_c \cdot \sqrt{u_{i-1}^2 + v_{i-1}^2}} \tag{7}$$

$$\theta_i = tan^{-1}(\frac{\Delta y_i}{\Delta x_i}) \tag{8}$$

NOTE: For complete details of the equations 2-8 see (Mudiyanselage, 2017).

Using this model, the overflow jet trajectory can be predicted. This allows for a simple analytical comparison. This analytical model will be tested against the experimental model.

Additional force on the caisson

The pressure distribution on the caisson during the overflow event can be seen in Figure 5. There is a distinct difference in the pressure distribution between the aerated and non-aerated cases. It is also important to note the difference between the water levels under the cavity in the two cases. As the water level under the cavity acts as a stabilizing force, the dynamics of the overflow jet, the pressure inside the cavity, and the water level under the cavity is critical in contributing to the stability of the caisson. The stark difference in the pressure distribution changes the force acting on the caisson. Using hydrostatic pressure distribution assumptions, the force on the caisson in the two cases can be given as described in Equation 9 (Mudiyanselage, 2017),

$$F = -\int_0^{d_t} \{[\rho_{eff} \cdot g \cdot (z - d_t)] - \Delta P\} \cdot B_c \cdot dz + \int_{d_t}^{H_c} \Delta P \cdot B_c \cdot dz, \tag{9}$$

where F [N] is the force on the caisson, d_t [m] is the water level under the cavity, ρ_{eff} $[kg/m^3]$ is the effective density in the water level under the cavity, g $[m/s^2]$ is the acceleration due to gravity, z [m] is the z coordinate, ΔP [Pa] is the pressure difference across the overflow jet in the non-aerated case, B_c [m] is the width of the caisson (width of the flume in this case), and H_c [m] is the height of the caisson. In the aerated case, Equation 9 can be simplified as $\Delta P = 0$ [Pa] and $\rho_{eff} = \rho_{water} = 1000$ $[kg/m^3]$. Using this formulation of the force on the caisson, the additional force generated due to the non-aeration can be simply assessed using Equation 10.

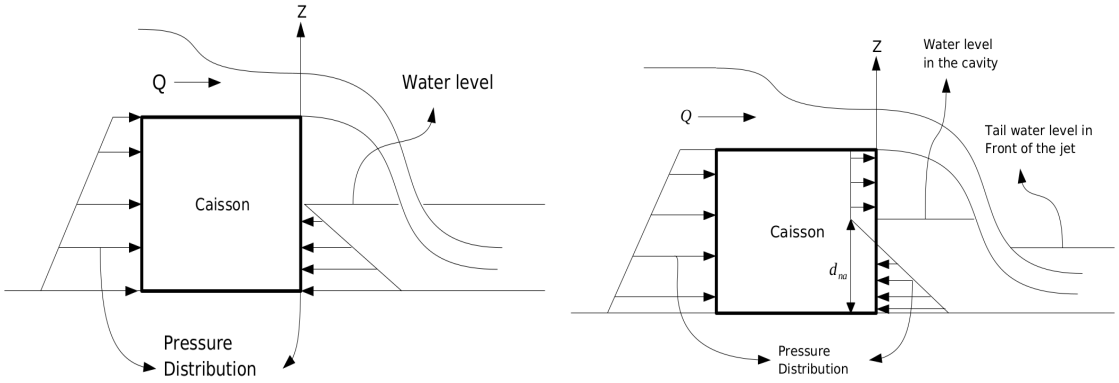

(a) Aerated case **(b) Non-Aerated case**

Figure 5: Forces acting on the caisson for the same overflow discharge quantities. The pressure distribution in the two cases are also depicted.

$$F_{ad} = F_{non-aerated} - F_{aerated}, \tag{10}$$

where F_{ad} is the additional force due to non-aeration, $F_{non-aerated}$ is the force on the caisson in the non-aerated case, and $F_{aerated}$ is the force on the caisson in the aerated case.

The above discussion motivates further investigation about over-topping of caisson. As a result, the following two approaches were considered to understand the dynamics of the flow:

- Experimental investigation
- Numerical investigation (using OpenFOAM)

Comparison of the two approaches along with the analytical formulation will provide sufficient insight about the overflow jet dynamics. This procedure also helps validate the numerical model for future use and detailed investigation for various parametric studies.

Experimental investigation

The experimental studies by Mudiyanselage (2017) were carried out at the Water Lab of the Civil Engineering and Geosciences faculty of the Delft University of Technology, The Netherlands. The selection of the geometric scale for carrying out the experimental investigation limits the overflow discharge conditions that can be 'replicated' in the flume. As a result, the selection of experimental geometric scale is crucial. The prototype model dimensions can be seen in Figure 6. For all the overflow discharge values the condition as described in Equation 11 has to be met,

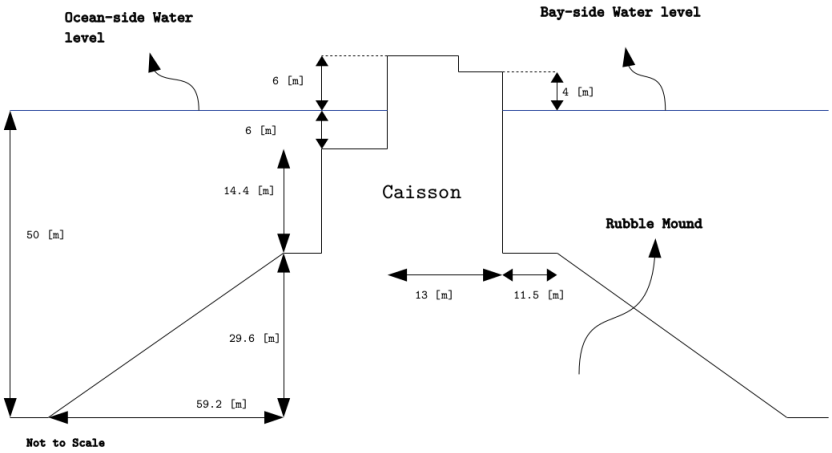

Figure 6: Dimensions of the caisson along with the rubble mound at the prototype scale.

$$H_{flume} > H_c + d_m, \tag{11}$$

where H_{flume} is the height/depth of the flume, H_c is the height of the caisson, and d_m is the maximum overflow depth over the caisson. Considering the prototype dimensions and available flume at the TU Delft Water Lab, a geometric scale of 1:150 was chosen (Mudiyanselage, 2017). The dimensions of the experimental flume available can be seen in Figure 7. As a scaled model is under investigation, not all physical processes correspond one-to-one in the scaled model. Hence, it is critical to assess which scaling law can be applied. In this case, three scaling parameters were considered (refer Table 1).

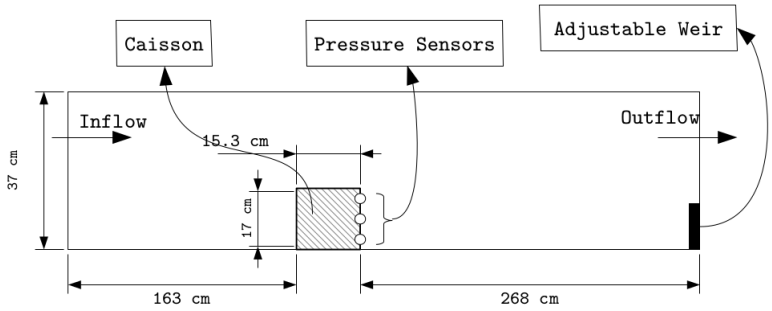

Figure 7: Experimental setup of the caisson overflow scaled model in the experimental flume at the Water Lab (side view). The width of the flume is 20 cm.

Table 1: Scaling parameters considered in the experimental studies. A comparison of the prototype and the scaled physical model are presented.

Scaling Parameter	Prototype	Scaled Physical Model
Reynolds Number = $\frac{UL}{\nu}$	$1.6 \cdot 10^6$	$1.5 \cdot 10^4$
Froude Number = $\frac{U}{\sqrt{gL}}$	0.2 - 1.5	0.2 - 1.5
Weber Number = $\frac{\rho U^2 L^2}{\sigma}$	$3.5 \cdot 10^4$	20

where, U = velocity [m/s], L = length scale (water depth) [m], ν = kinematic viscosity of the fluid = 10^{-6} $[m^2/s]$, g = gravitational acceleration = 9.81 $[m/s^2]$, ρ = density of the fluid = 1000 $[kg/m^3]$ and σ = Surface tension = 0.007286 $[N/m]$.

As seen in the Table 1, the only scaling parameter consistent in both the cases is the Froude (Flow regime) scaling parameter. There is a large disparity between the Reynolds (Turbulence) and Weber (Surface Tension) scaling. As the limit for turbulent flow is not sharply defined for open channel flows, a value for $Re > 2000$ is considered to be turbulent (Spurk and Aksel, 2008). As a result, the experimental investigations complies with the right turbulent flow regime. However, the Weber scaling can certainly have an effect in the modeling of the problem. The limit for which surface tension can be neglected is ~ 120 (Peakall and Warburton, 1996). Due to the lack of data about the effects of surface tension on overflow jets, the assessment of the influence of Weber scaling is not considered in this case. This possible influence of surface tension can be simulated in the numerical model (Mudiyanselage, 2017). The Froude scaling was used to scale the flow physics. Artificial aeration in the cavity is introduced once the flow enters the steady state condition. This is done in order to assess the difference in the overflow jet trajectory for the aerated and non-aerated cases. The discharge is measured using a downstream sharp-crested weir. In total 10 overflow discharge values were studied (see Mudiyanselage (2017) for details).

The pressure sensors used in the experiment are of 'differential' type. For the experiments, one end of the pressure sensor is always connected to the atmosphere. As a result, the pressure readings are relative to the atmospheric pressure. As the top pressure sensor is always in contact with air (inside the cavity), the accuracy of the sensor is not reliable. A similar situation exists for the sensor in the middle (see Figure 7). Hence, only the lowest pressure sensor readings have been considered. The pressure distribution in the non-aerated case can be seen in Figure 5b. Assuming the hydrostatic pressure in the water level under the cavity, the pressure difference (ΔP) can be estimated using the water level difference. This formulation is as described in Equation 12 (see Mudiyanselage (2017) for a complete derivation),

$$\Delta P = (\overline{P_{3a}} - \overline{P_{3na}}) + \overline{d_{na}} \cdot \rho_{eff} \cdot g, \tag{12}$$

where P_{3a} and P_{3na} are the pressure sensor readings for the lowest sensor in the aerated and the non-aerated cases respectively, $\overline{d_{na}}$ is as defined in Figure 5b and the other parameters are as defined earlier.

Effective density inside the cavity

Using the analytical and experimental formulation as discussed above, the overflow jet trajectories were compared. It was observed that the two trajectories as predicted by the analytical method and the one observed in the experiments did not agree with each other (see Mudiyanselage (2017) for details). It was hypothesized that the effective density in the cavity is not constant which leads to the deviation between the two trajectories (analytical and experimental). This hypothesis is consistent due to the fact that there is vigorous bubbling under the overflow jet in the non-aerated case. In order to investigate this behavior of water level in the cavity, an integral momentum conservation analysis was conducted with the control volume as seen in Figure 8.

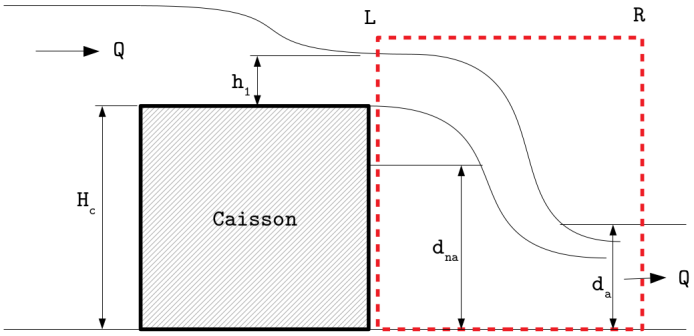

Figure 8: Control volume used for momentum conservation analysis based on the dimensions of Figure 7.

Formulating and solving the momentum equation over this control volume for the cavity sub-pressure yields Equation 13,

$$\Delta P = \frac{\frac{1}{2}\rho g B(h_1^2 - d_a^2) + \frac{1}{2}\rho_{eff} g B d_{na}^2 - \frac{\rho Q^2}{B}(\frac{1}{d_a} - \frac{1}{h_1})}{BH_c}, \tag{13}$$

where all the length scales are as defined in Figure 8, and B is the width of the the flume. This conservation of momentum analysis also shows that an effective water density of 800 kg/m^3 under the nappe brings theory into agreement with measurements, as shown in Figure 9. Together with the nappe deflection of Figure 10, this adds some confidence to the hypothesis that air entrainment and bubbling in the water under the nappe might contribute significantly to the dynamics of non-aerated nappe overflow. Assuming hydrostatic forces on both sides of the caisson during overflow using measured values of ΔP from Equation 12, nappe non-aeration resulted in an average of 9% and a maximum of 14% greater sliding force than the aerated cases experienced in the tests conducted.

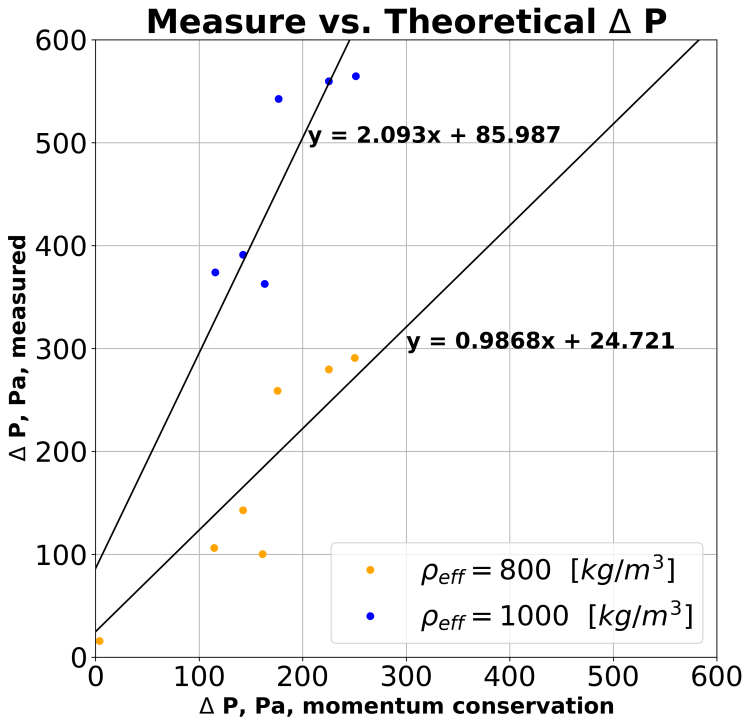

Figure 9: Measured (Equation 12) vs. theoretical (Equation 13) cavity sub-pressures for all experimental tests of Mudiyanselage (2017).

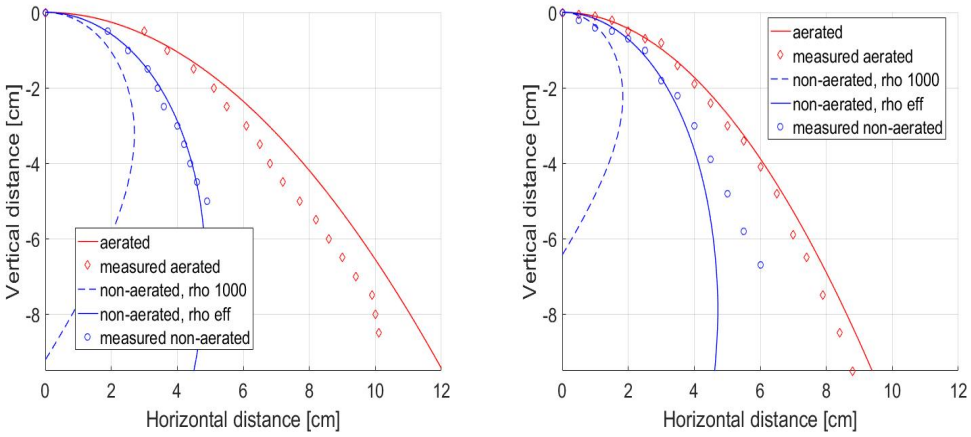

(a) Test 3 overflow jet trajectory comparison **(b) Test 10 overflow jet trajectory comparison**

Figure 10: Measured and modeled nappe trajectories at two different flow rates. The value for rho eff is $\rho_{eff} \sim 800$ [kg/m^3].

This density change inside the water level under the cavity will also be considered in the numerical model. For consistent comparison, the trajectory results from this momentum analysis and the experimental results will be compared with the numerical model. From this section onwards the term '*analytical result*' will refer to the trajectory results using the effective density analysis as discussed in the above section.

Numerical investigation

In order to have complete flexibility and reliability of the numerical model, OpenFOAM was selected. Specifically, the interFoam solver was used to simulate the flow over the caisson. The interFoam solver has numerous validations for free surface flows. Some of them are as cited here in the studies by (Higuera et al., 2013), (Deshpande et al., 2012) and (Lopes, 2013). With motivation from these studies, an in depth modeling of the flow over caisson was considered. The numerical model was used to replicate the experimental studies carried out by Mudiyanselage (2017). The model geometry is the same as the experimental model investigation as seen in Figure 7. For the detailed numerical setup, see Patil (2018).

The system of equations solved in the numerical model are presented in Equations 14 - 17. Additional equations for the transport of k (Turbulent kinetic energy $[m^2/s^2]$) have to be solved as well. The turbulence closure used in this model was the standard $k-\epsilon$ turbulence model, where ϵ is the rate of dissipation of turbulence energy $[m^2/s^3]$. Further details about the standard $k-\epsilon$ turbulence closure can be found in the seminal paper by Launder and Spalding (1974).

$$\nabla \cdot (\overline{\mathbf{u}}) = 0 \tag{14}$$

$$\frac{1}{\rho}\left(\frac{\partial \bar{u}_i}{\partial t} + \bar{u}_j \frac{\partial \bar{u}_j}{\partial x_j}\right) = \frac{\partial}{\partial x_j}\left[- \bar{p}\delta_{ij} + \mu\left(\frac{\partial \bar{u}_i}{\partial x_j} + \frac{\partial \bar{u}_j}{\partial x_i}\right) - \rho\overline{u_i' u_j'}\right] \tag{15}$$

$$\frac{D}{Dt}(\rho k) = \nabla \cdot (\rho D_k \nabla k) + G_k - \frac{2}{3}\rho(\nabla \cdot \overline{u})k - \rho\epsilon + S_k \tag{16}$$

$$\frac{D}{Dt}(\rho\epsilon) = \nabla \cdot (\rho D_\epsilon \nabla \epsilon) + \frac{C_1 G_k \epsilon}{k} - (\frac{2}{3}C_1 - C_{3,RDT})\rho(\nabla \cdot \overline{u})\epsilon - C_2\rho\frac{\epsilon^2}{k} + S_\epsilon \tag{17}$$

NOTE: Please refer the official OpenFOAM documentation for the details OpenCFD (2018). The turbulence model equations presented above are for compressible flows.

where $\nabla\cdot$ is the divergence operator, $\overline{\mathbf{u}}$ is the mean velocity vector field, ρ is the density of the fluid, $\overline{u_i}$ is the i^{th} mean velocity component, x_j is the j^{th} space coordinate, $\overline{p}$ is the mean scalar pressure field, δ_{ij} is the Kronecker delta, and μ is the dynamic viscosity of the fluid.

The interFoam solver employs a simple approach to differentiate between the two fluids (air and water in this case). The alpha (α) fraction can take any value between 0 and 1. As a result, if the computational cell has an alpha value of 1 means it is completely filled with water and if it has an alpha value of 0 it implies that the cell is completely filled with air. Using this simple methodology, the multiphase simulation can be setup. The governing equations and other details can be seen in Deshpande et al. (2012).

RESULTS AND DISCUSSION

Convergence of the numerical model

In order to have reliability of the numerical model results, the very first step in the validation process involves confirmation of convergence. This convergence history can be obtained for all the computed quantities. In this case the computed quantities are pressure (p_{rgh}), turbulent kinetic energy (k), and the rate of turbulent energy dissipation (ϵ). The convergence history was obtained using the OpenFOAM runtime utility. From Figure 11, it is evident that the normalized residuals are below the accuracy limit (10^{-3}). This confirms the convergence of the numerical model for the given physical model. All the numerical models were observed to have a similar convergence history.

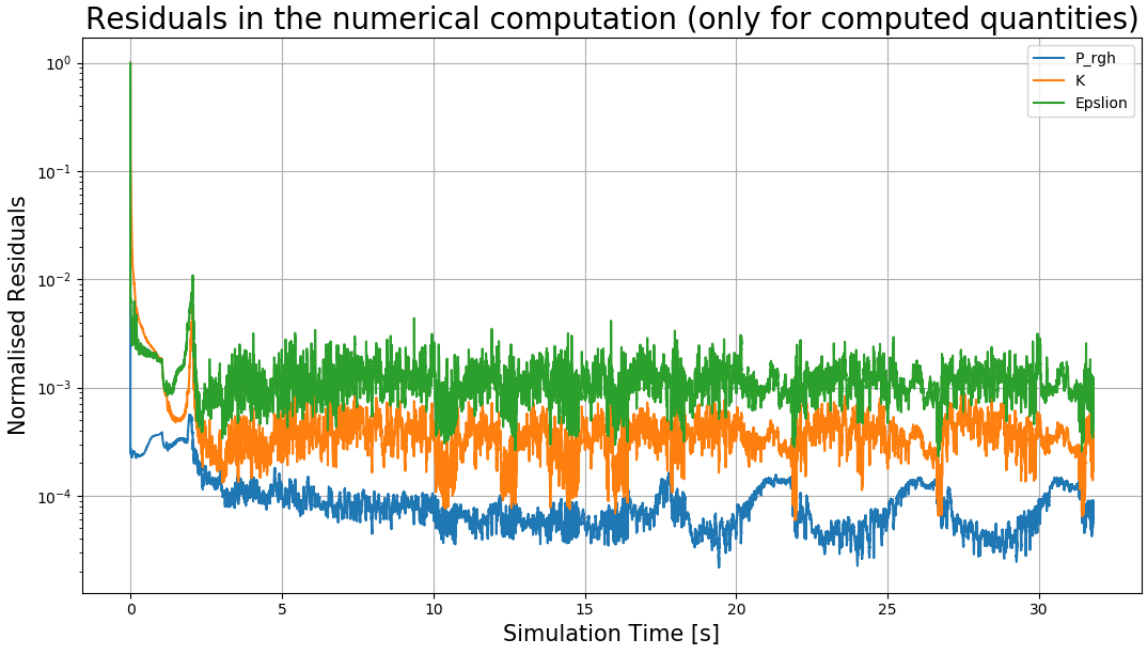

Figure 11: Residuals time series for test 10 for about 35 s of the simulation.

Grid sensitivity

Three grids were checked for appropriate capture of the air-water interface. The grids which were compared to assess the grid sensitivity have been presented in Table 2.

Table 2: Grid sizes compared in order to assess the sensitivity of the numerical model to capture the air-water interface.

Grid Name	Grid Resolution
Grid 1	1 cm
Grid 2	0.4 cm
Grid 3	0.2 cm

Visual inspection of the results (see Figure 12) shows that a grid resolution of 1 cm cannot appropriately

resolve the overflow jet. Consequently, this grid cannot be considered for further investigations. In order to check the behavior of the grids with a resolution of 0.4 cm and 0.2 cm, a direct comparison was made. The validation process includes the ability of the grid size to capture the size and the trajectory of the overflow jet appropriately. These trajectories have been compared with the experimental results. The validation of the numerical model has been presented in the next section.

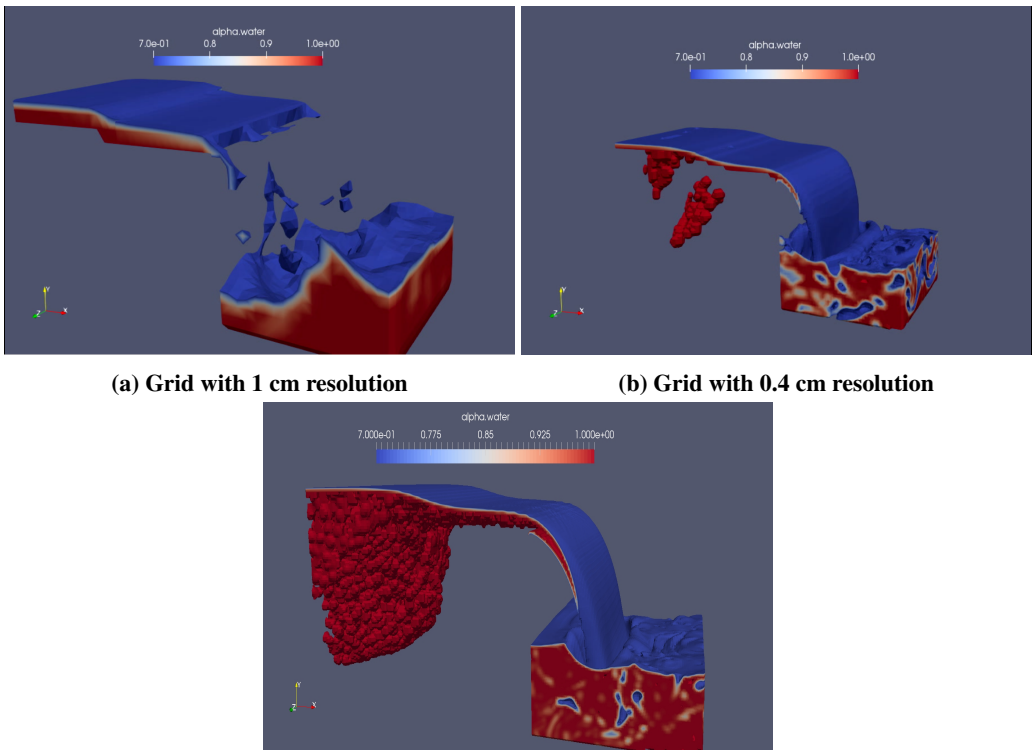

(a) Grid with 1 cm resolution **(b) Grid with 0.4 cm resolution**

(c) Grid with 0.2 cm resolution

Figure 12: Overflow jet behavior with different mesh sizes ($Q = 0.0025\ [m^3/s]$). The overflow jet has been resolved using a water fraction higher than 0.7.

Validation of the numerical model

The numerical model results have been validated against the experimental studies and the analytical model. Before a direct comparison is made, it is important to discuss the overflow jet behavior in the numerical model for the non-aerated case. As seen in Figure 13, the overflow jet does not stay as a steady stream of fluid. With time, the cavity under the overflow jet shrinks as a result of air entrainment. This reduces the pressure inside the cavity until the point where the overflow jet cannot retain its original shape. The reduction in pressure inside the cavity results in a progressive rise of the water level and pulling of the overflow jet towards the caisson wall. The curvature of the jet increases until the jet breaks at the sides and hugs the wall of the caisson completely. This provides a means of aeration back into the cavity at the sides of the flume and the overflow jet retains its original position by virtue of the incoming horizontal momentum. This cycle of air entrainment from and into the cavity continues throughout the simulation period. As a result, the overflow jet trajectory cannot be directly compared to the numerical model results. In order to provide a detailed representation of the jet behavior, three positions of the overflow jet have been presented. The three positions correspond to furtherest, mean and closest position of the overflow jet in comparison to he caisson wall.

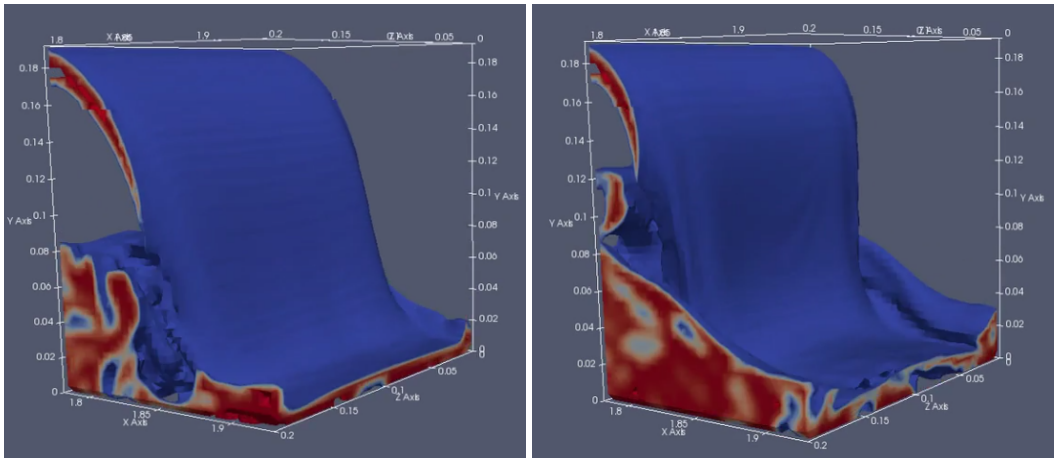

(a) Nappe far end position (t = 18.5 [s]). **(b) Nappe mid position (t = 19 [s]).**

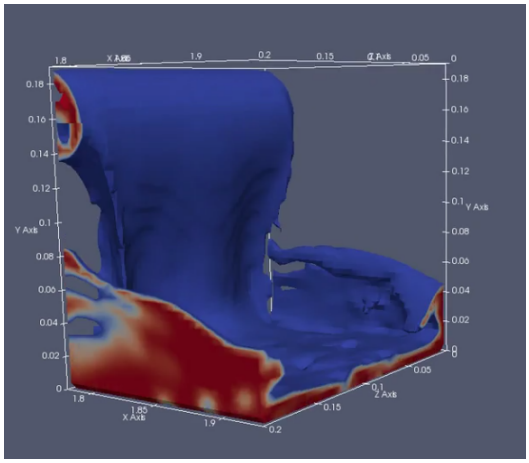

(c) Nappe hugging the caisson wall (t = 22 [s]).

Figure 13: Non-aerated nappe behavior for grid resolution of 0.2 cm (Test3 $Q = 0.00405\ [m^3/s]$). This behavior is cyclic, and the nappe flutters about the mid position. The time at which the overflow jet position is recorded depends on the write time specified in the numerical model.

The validation results have been obtained from a longitudinal slice of the 3-D numerical model along the center of the flume. The results for test10 with a grid resolution of 0.4 cm can be seen in Figure 14. Due to limited grid resolution, the size of the overflow jet and the trajectory are not resolved appropriately. Hence, the results for this mesh size were considered to be not appropriate for capturing the overflow jet trajectory. Considerable improvement in the trajectory and the size of the overflow jet was observed in the grid with resolution of 0.2 cm numerical results (see Figure 15). The overall size and the trajectory have been resolved adequately. Moreover, the results correspond very well with the experimental and the analytical models.

Similar results have been obtained for test 3. The grid with a resolution of 0.4 cm fails to adequately capture the trajectory and size of the overflow jet (see Figure 16). As observed in the test 10 results, considerable improvement in the trajectory and size of the overflow jet can be observed in the grid with a resolution of 0.2 cm (see Figure 17). It is important to note the difference between the water levels in the four figures presented in this section. The change in overflow jet trajectory and the rise of the water level as a result of the decrease in pressure inside the cavity are clearly visible. As the numerical results with a grid resolution of 0.2 cm show promising results, this grid was selected for all the final computations in the numerical investigations.

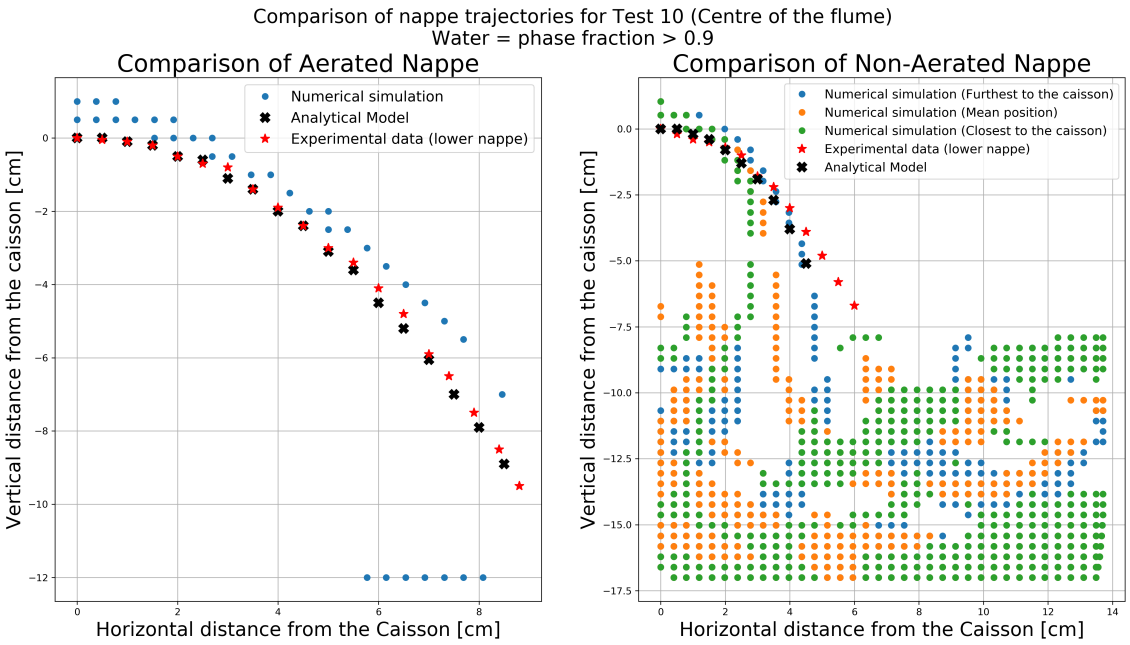

Figure 14: Test 10 nappe validation results with grid resolution of 0.4 cm. The effective density in the analytical model is 800 kg/m^3.

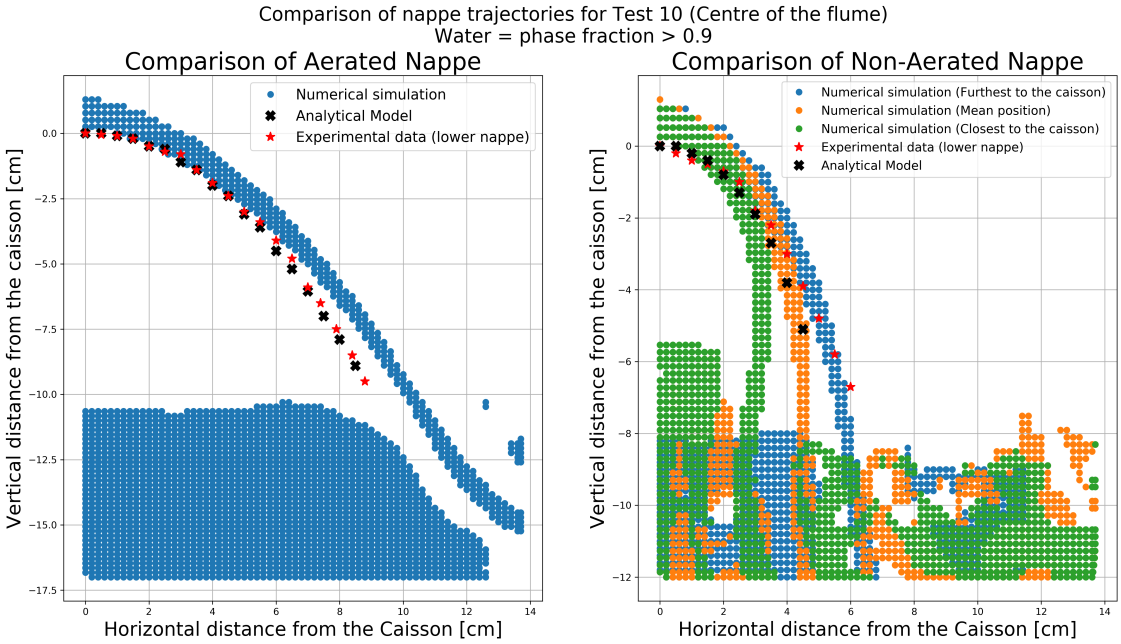

Figure 15: Test 10 nappe validation results with grid resolution of 0.2 cm. The effective density in the analytical model is 800 kg/m^3.

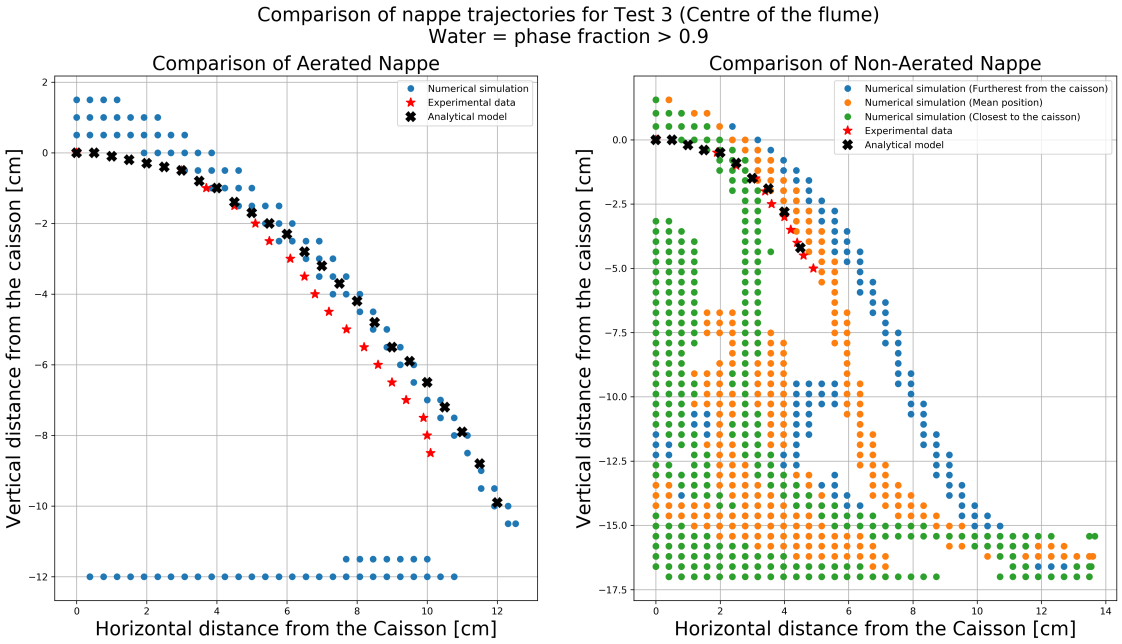

Figure 16: Test 3 nappe validation results with grid resolution of 0.4 cm. The effective density in the analytical model is 800 kg/m^3.

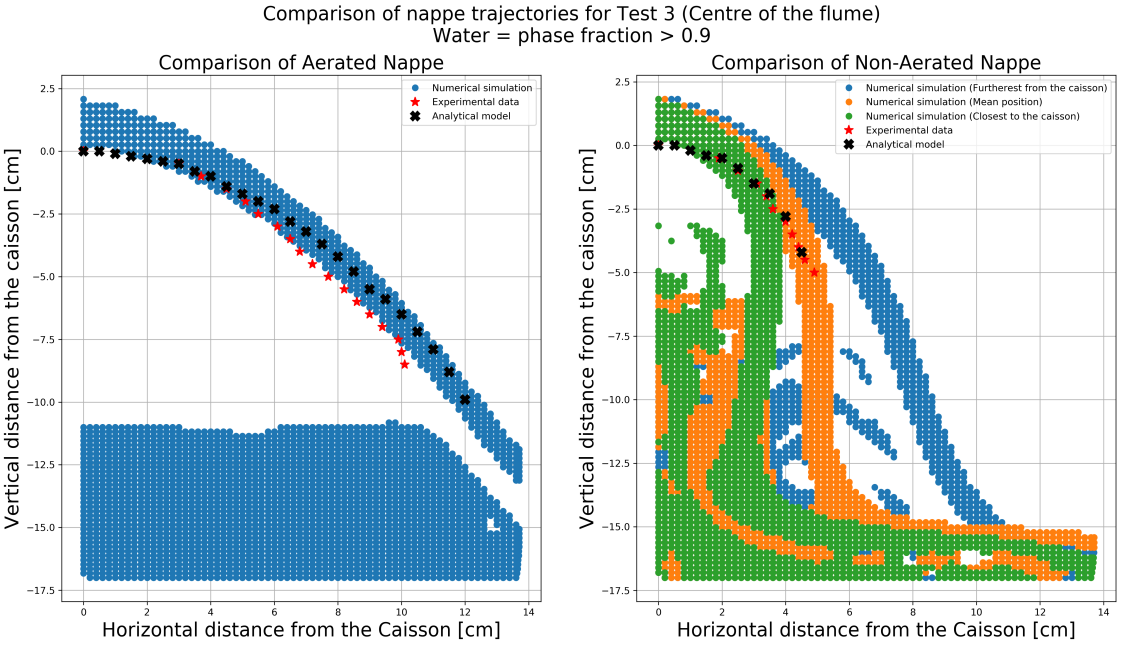

Figure 17: Test 3 nappe validation results with grid resolution of 0.2 cm. The effective density in the analytical model is 800 kg/m^3.

Water fraction inside the cavity

The water level under the cavity provides a stabilizing force for the caisson. As a result, the behavior of pressure distribution affects the stability of the caisson. The hydrostatic pressure equation is given as follows:

$$P = \rho \cdot g \cdot h, \tag{18}$$

where P is the pressure [Pa], ρ is the density of the fluid [kg/m^3], g is the gravitational acceleration [m/s^2], and h is the depth under the free surface [m]. Using this formulation, the pressure distribution can be scaled by density. As a result, assessment of the effective density inside the cavity has important implications on the pressure distribution.

In order to have a consistent reference volume for the calculation of water fraction, the block as defined in Figure 18 was used for all cases. As the water level is highly variable (see Figure 17), a reference volume that is consistent for all the 6 cases had to be considered.

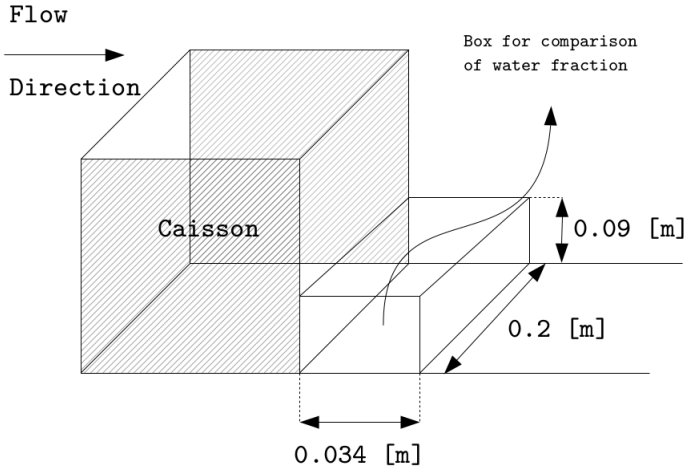

Figure 18: Schematic for water fraction computation volume in the domain

The effective density is simply computed using the Equation 19,

$$\rho_{eff} = \alpha_{water} \cdot \rho_{water}, \tag{19}$$

where ρ_{eff} is the effective density [kg/m^3], α_{water} is the average water fraction over the reference volume [-], and ρ_{water} is the density of water $\sim$ 1000 [kg/m^3]. The highly temporal behavior of the overflow jet was not anticipated in the numerical model. As a result, a runtime routine in OpenFOAM was not employed to obtain a time series of this block. This highly temporal behavior of the water level inside the cavity hinders drawing any conclusion about the behavior of the effective density inside the cavity for both the cases. Table 3 presents the effective density for the three conditions of overflow jet with two tests. The analytical results propose an effective α_w value of about 0.8, which is higher than observed in a block average at one instance for different positions of the overflow jet. However, it is interesting to note that the variation of α_w and that the magnitude of $\alpha_w < 1$.

Table 3: Effective water fraction under the cavity. The values presented are block averages.

Position of the nappe	**Test 10** (α_w)	**Test 3** (α_w)
Closest to the caisson	0.6547	0.6649
Mean position	0.8398	0.6209
Furthest from the caisson	0.6433	0.6192

Force on the caisson

The basic idea for computing the force in the numerical model is applying static equilibrium to compute the unknowns. Figure 19 shows all active forces on the caisson block for the non-aerated case. The only difference in the aerated case would be the pressure distribution on the downstream face of the caisson. The results for test 3 are presented below (see Figure 20). Similar time series behavior was obtained for other test cases. It is interesting to see how the force for the aerated and the non-aerated case behave

almost identically during the first 2.5 s of simulation time (see Figure 20). As the initial water level inside the cavity in both the cases is the same, the force on the caisson does not vary until the dynamics of the non-aerated overflow jet start generating additional force on the caisson. After about 3 s of simulation time, the dynamics of the non-aeration start playing a big role. Due to the entrainment cycle (as discussed previously), the force on the caisson has a cyclic behavior. This is one of the key results that could not be obtained in the experimental investigation. The stability of the caisson can be affected to a large extent as a result of this oscillating force. This high frequency fluctuating force has its peak just after the overflow jet leaves the caisson wall (last stage in figure 13). This was confirmed by correlating the pressure inside the water level in the cavity with the overflow jet position for the same test, which exactly mirrors the behavior in the pressure time series. The details for the pressure time series can be found in Patil (2018).

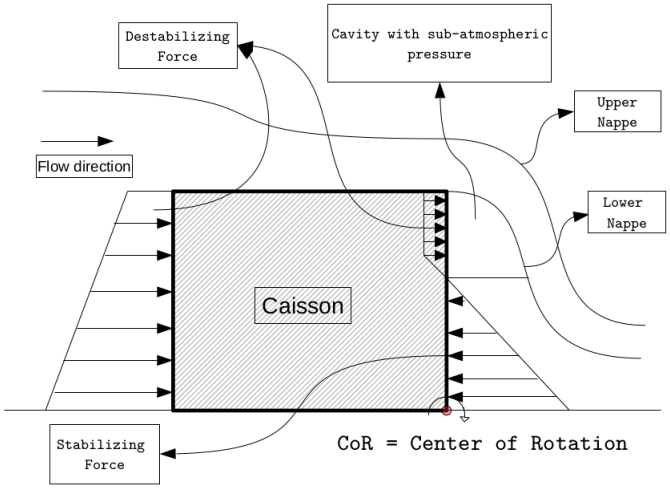

Figure 19: Simplified sketch of the forces acting on the caisson during over-topping. Only horizontal forces have been considered in the static balance.

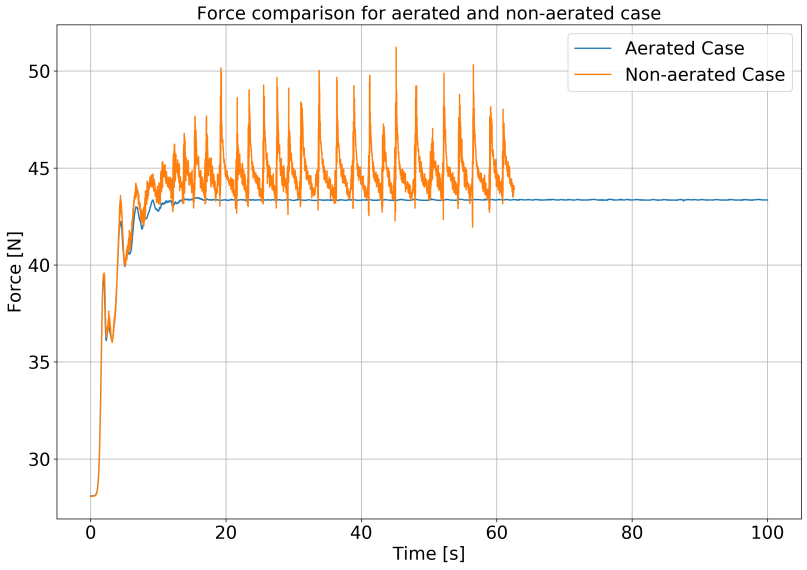

Figure 20: Comparison of force on the caisson for test 3 with $Q = 0.00405\ m^3/s$. The force in the figure represents the net force on the caisson in the numerical model.

For the design case, the maximum forces acting on the caisson in the aerated and non-aerated cases

govern the stability of the caisson. Thus, using the Equation 9, and applying a *max* function to this equation can give a general trend for the additional force in each case. The additional force generated in this study are as described in Table 4.

Table 4: Additional force for various tests carried out in the study using a grid resolution of 0.4 cm.

Overflow discharge [m^3/s]	Initial water level in the cavity [cm]	Aerated Case [N]	Non-aerated Case [N]	Additional Force [N]
0.0025	6.4	39.77	38.95	-0.82
0.0028875	5.4	40.79	40.475	-0.315
0.003275	5.4	41.71	40.48	-1.23
0.0036625	1.5	42.72	46.105	3.385
0.00405	1.5	43.47	51.23	7.76
0.0044375	1.5	44.323	52.685	8.362

It was observed that the force on the caisson does not differ much, between grid with 0.4 cm and 0.2 cm resolution. Therefore, in order to have sufficient data, and minimize computational time, the results for further investigations were carried out using the grid with a resolution of 0.4 cm for the force computations. It is clear that the water level in the cavity plays an important role in this system. The need for validation of the numerical model forced the different water levels to be simulated for different discharge levels. However, as some of the tests were not considered in the experimental investigations, a constant water level under the cavity was implemented. The initial water level was set to 1.5 cm as it was observed that the overflow discharge can completely submerge the downstream region. This made it difficult to observe the force on the caisson correctly. Accordingly, a low initial water level was initialized.

CONCLUSIONS AND RECOMMENDATIONS

As part of this comprehensive study, it was observed that non-aeration of the cavity under the nappe can lead to additional force on the caisson in certain situations (See table 4). The experimental investigation suggest that non-aeration could add about 15-30% additional horizontal force on the caisson. As a result, the non-aeration of the overflow jet can jeopardize the sliding stability of the caisson. Although, the experimental investigations suggest the efficacy of the analytical method, scale effects can have significant impact on the system. The effect of ΔP was found to be larger than that of the effect of surface tension (Mudiyanselage, 2017), the Weber scaling could influence the air entrainment process and affect the air distribution (thus the effective density ρ_{eff}) inside the water level under the cavity. The analytical model predicts the overflow jet trajectory sufficiently well. However, in order to estimate the trajectory correctly, the inclusion of effective density should be considered. The analytical formulations agree well with the experimental (and numerical) results. The validity of the hydrostatic assumption could not be verified due to limitations in the physical and the numerical model setup. Further focus on this aspect is required to ascertain the analytical model calculations as presented in this study.

The numerical model studies indicate that the interFoam solver performs adequately to resolve the overflow jet trajectory. The model agrees well with the experimental studies and the analytical model results. Numerical model predictions suggest that non-aeration can result in an additional force of about 8-19% in comparison to the aerated case for the overflow discharges as presented in Table 4. It was observed that the water level inside the cavity has a large effect on the stability of the caisson. The numerical results have been improved drastically in comparison to the previous studies by Bricker et al. (2013) and Mudiyanselage (2017). The modeling of overflow jet using a simple $k-\epsilon$ based model provides a reasonable solution field without any additional change in the turbulence model, thus disproving the hypothesis stated in Bricker et al. (2013) about the inability of $k-\epsilon$ model to resolve flow field for this application. As discussed earlier, the physics of the aeration of the overflow jet is highly 3-dimensional. A 2-dimensional numerical model cannot incorporate the overflow jet dynamics correctly. This also confirms why the earlier studies by Mudiyanselage (2017) could not model the non-aerated overflow jet appropriately. Consequently, only a 3-dimensional model (such as the one used in this study) can correctly model the physical behavior of the non-aerated overflow jet. Additionally, the pressure drop across the jet due to non-aeration changes the dynamics of the water level under the cavity. It was observed that due to non-aeration the water level inside the cavity has a different effective density (on average) in comparison to the aerated counterpart for

the same overflow discharge. This suggests there is a deviation from the expected pressure distribution using the analytical model (Patil, 2018). However, due to lack of detailed investigation, no conclusions can be drawn about the pressure distribution and its implications on the stability of the caisson. This calls for further research into the water level behavior and its effect on the stability of the caisson. One of the crucial results from the numerical investigations is the nature of the force on the caisson. It was observed that the force on the caisson is not steady but cyclic/oscillatory in nature. This has a larger impact on the dynamics of the fluid-structure interaction. The cyclic load can dislodge the caisson blocks easily which could explain the observations during the tsunami event in 2011.

Despite the improved performance of the 3-D simulation over the 2-D simulation, there is still a distinct difference between the numerical and the experimental behavior of the overflow jet. The overflow jet oscillates with higher frequency and amplitude in the numerical model compared to the experimental observations. This suggests that the numerical model lacks an aeration mechanism that exists in the experimental investigation. The plausible explanation for this is the inability of interFoam to capture small bubbles that are entrained and supplied back into the non-aerated cavity. It was observed in the experimental studies that the overflow jet (non-aerated) breaks only at the lower-sides (near the flume walls) of the flume and draws in air to aerate the cavity. However, the numerical model suggests that the overflow jet itself breaks and hugs the caisson wall completely (test 3), draws in air and returns to its original location. This stark contrast in the dynamics needs to be addressed in terms of computational methodology employed for studying overflow type behavior. The inability of interFoam solver to resolve detailed air-entrainment related physics could easily question the validity of the numerical results especially for high overflow discharges. This inability could also be attributed to the turbulence model employed in the numerical model. As Reynolds Averaged Navier-Stokes modeling technique was used, the resolution of small scale turbulent features can directly lead to the inability to model air-water interactions smaller than the model dictates. Although the numerical results suggest sufficient applicability to resolve mean flow features, the stark contrast in the overflow jet behavior in the numerical and experimental investigations suggests that the small-scale physics has not been resolved, which affects the overall behavior of the overflow jet (especially the aeration mechanism). In conclusion, a word of caution has been advised to model overflow physics using interFoam and the standard $k - \epsilon$ model. Hence, detailed investigation is recommended to investigate the air-entrainment physics using either a Large Eddy type simulation or inclusion of the air-entrainment physics.

References

M. Abdalla and M. Shamaa. Experimental investigations of nappe profile and pool depth for broad crested weirs. *International Journal of Engineering Research and General Science*, 4(1), 2016.

T. Arikawa, M. Sato, K. Shimosako, T. Tomita, D. Tatsumi, G.-S. Yeom, and K. Takahashi. Investigation of the failure mechanism of the kamaishi breakwater due to tsunami, initial report focusing on hydraulic characteristics. *Technical note of the Port and Airport Research Institute*, 2012.

J. Bricker, H. Takagi, and J. Mitsui. Turbulence model effects on vof analysis of breakwater overtopping during the 2011 great east japan tsunami. *Proceedings of the 2013 IAHR World Congress*, 10153, 2013.

H. Chanson. *Air Bubble Entrainment in Free-Surface Turbulent Shear Flows*. Academic Press, 1996.

V. T. Chow. *Open Channel Hydraulics*. Blackburn Press, 2009.

S. S. Deshpande, L. Anumolu, and M. F. Trujillo. Evaluating the performance of the two-phase flow solver interfoam. *Computational Science and Discovery*, 5(1):014016, 2012. URL `http://stacks.iop.org/1749-4699/5/i=1/a=014016`.

P. Higuera, J. L. Lara, and I. J. Losada. Simulating coastal engineering processes with openfoam. *Coastal Engineering*, 71:119 – 134, 2013. ISSN 0378-3839. doi: https://doi.org/10.1016/j.coastaleng.2012.06.002. URL `http://www.sciencedirect.com/science/article/pii/S0378383912001093`.

B. E. Launder and D. B. Spalding. The numerical computation of turbulent flows. *Computational methods in Applied Mechanics and Engineeering*, 3-2:269–289, 1974.

P. M. B. Lopes. Free-surface flow interface and air-entrainment modelling using openfoam. 2013. [Accessed Online], "https://estudogeral.uc.pt/bitstream/10316/24534/1/Pedro%20Lopes_%20Free-surface%20flow%20interface%20and%20air-entrainment%20modelling%20using%20OpenFOAM_FINAL.pdf".

J. Mitsui, A. Matsumoto, M. Hanzawa, and K. Nadaoka. Stability of armor units covering rubble mound of composite breakwaters against a steady overflow of tsunami. *Coastal Engineering Proceedings*, 28, 2014.

S. Mudiyanselage. Effect of nappe non-aeration on caisson sliding force during tsunami breakwater overtopping, 2017. [Online], "https://repository.tudelft.nl/islandora/object/uuid:728416ce-fa4e-4459-ac56-2059b2fc10c3?collection=education".

OpenCFD. Extended code guide. https://www.openfoam.com/documentation/cpp-guide/html/index.html, 2018.

A. Patil. Numerical investigation of the effect of nappe non-aeration on caisson sliding force during tsunami breakwater over-topping using openfoam. *TU Delft repository, student theses*, 2018. [Online], "https://repository.tudelft.nl/islandora/object/uuid%3A65aff400-8610-4867-92fa-ca33a9e54a01?collection=education".

J. Peakall and J. Warburton. Surface tension in small hydraulic river models-the significance of the weber number. *Journal of Hydrology, New Zeland*, 35, 1996.

J. Spurk and N. Aksel. *Fluid Mechanics*. Springer, 2008. doi: 10.1007/978-3-540-73537-3.

A. Suppasri, P. Latcharote, J. D. Bricker, N. Leelawat, A. Hayashi, KeiYamashita, F. Makinoshima, V. Roeber, and F. Imamura. Improvement of tsunami countermeasures based on lessons from the 2011 great east japan earthquake and tsunamiâ"situation after five years. *Coastal Engineering*, 58(04):1640011., 2018.

H. Takagi and J. Bricker. Breakwater damage and the effect of breakwaters on mitigation of inundation extent during tsunami's: Case study of the 2011 great east japan earthquake and tsunami. *Handbook of Coastal Disaster Mitigation for Engineers and Planners*, pages 363–383, 2015.

H. Takahashi, S. Sassaa, Y. Morikawaa, D. Takanoa, and K. Maruyama. Stability of caisson-type breakwater foundation under tsunami-induced seepage. *Elsevier journal of Soils and Foundations*, 54, 2014.